Virtual wave flume and Oscillating Water Column modeled by lattice Boltzmann method and comparison with experimental data

Thorimbert, Yann; Latt, Jonas; Cappietti, Lorenzo; Chopard, Bastien

How to cite

THORIMBERT, Yann et al. Virtual wave flume and Oscillating Water Column modeled by lattice Boltzmann method and comparison with experimental data. In: International Journal of Marine Energy, 2016, vol. 14, p. 41–51. doi: 10.1016/j.ijome.2016.04.001

This publication URL: https://archive-ouverte.unige.ch/unige:106934
Publication DOI: 10.1016/j.ijome.2016.04.001

Virtual Wave Flume and Oscillating Water Column modeled by Lattice Boltzmann Method and comparison with experimental data

Yann Thorimbert[a], Jonas Latt[a], Lorenzo Cappietti[b], Bastien Chopard[a]

[a] *University of Geneva*
Centre Universitaire d'Informatique
7, route de Drize
1227 Carouge
Switzerland
Corresponding author phone: +41223790208
[b] *University of Florence*
Department of Civil and Environmental Engineering
Via S.Marta 3, 50139 Firenze
Italy

Abstract

In this paper, a novel approach for simulating Oscillating Water Column (OWC) using lattice Boltzmann method (LBM) is presented. A direct comparison between a real wave flume and a 3D-Large Eddy Simulation (LES) numerical lattice Boltzmann (LB) wave flume is developed through the analysis of an OWC energy converter in order to validate the LBM approach for simulating OWCs. The numerical model uses a Volume-of-Fluid (VOF) approach and handles the water-air coupling into the OWC air chamber. The experimental and numerical setup are described. Comparisons for water level during free oscillation test, water level and air pressure under regular wave attacks are given and show that the LB model is accurate. We also discuss the efficiency of the simulated OWC. The 3D numerical model offers a powerful tool in order to study the 3D phenomena occurring into OWCs.

Keywords: Oscillating Water Column, lattice Boltzmann, wave energy converter, Free Surface model, Volume-of-Fluid, numerical wave flume

1. Introduction

In oceans and seas, surface waves due to wind represent a considerable amount of energy [1], as shown for example in [2] for the italian offshore and

Email addresses: yann.thorimbert@unige.ch (Yann Thorimbert), jonas.latt@unige.ch (Jonas Latt), lorenzo.cappietti@unifi.it (Lorenzo Cappietti), bastien.chopard@unige.unige.ch (Bastien Chopard)

[3] for the case of the Mediterranean sea. To take advantage of this available energy, several types of wave energy converters (WEC), including OWC, can be considered (see [4, 5] for a detailed review of the avalaible WEC technologies).

OWC devices comprise a partly submerged structure, containing an air chamber whose bottom is open below the water surface. The incident waves trigger the oscillating motion of the internal free surface, causing the air inside the chamber flow through a turbine that drives an electrical generator. Note that due to the oscillating motion of the water surface, the air flow is bidirectional and one needs to use a self-rectifying turbine or a turbine with rectifying valves in order to capture maximum energy [6, 7]. A common choice for the Power-Take-Off (PTO) system is the Wells turbine [8].

Although some full size power plant have already been tested as for instance in Mutriku in Spain[9] or LIMPET project in Scotland [10], OWCs remain mainly experimental devices for the moment and multiple experiments are performed to investigate air turbines, high-pressure hydraulics, linear electrical generators and mooring systems. [11].

Many efforts on numerical modeling of OWC have been done so far, such as time and frequency-domain[12], 2D Reynolds-Averaged Navier-Stokes (RANS) approach [13], 3D RANS approach [14], or 3D CFD simulation using FLUENT with a Volume-of-Fluid (VOF) method [15] or OpenFOAM with a multiphase, VOF model [16]. To the best of our knowledge, LBM has never been applied to the simulation of an OWC; we propose here a fully 3D-LES approach based on LBM.

The aim of this study is to build a LBM model for simulating an OWC test into a virtual flume and to compare the simulation results with experiments in order to evaluate the model's capability and accuracy to simulate the interaction of water waves with OWC. Thanks to its exceptional capacity to parallelize on many cores [17], LBM is a good choice when large computational effort is needed. For instance, if the entire system constituted of many OWCs on a very large floating structure is to be simulated, or for simulating OWC with complex shapes, LBM is potentially a candidate, and the study of its capability is of particular interest. While the outcome of this study is to validate the model for fixed OWC with given PTO, the long term objective is to develop a LBM wave-flume and use it as a virtual laboratory for the studies of the OWC devices.

2. Laboratory experiments

The experiments on the OWC physical model were performed in the wave-current flume of the Laboratory of Maritime Engineering at Florence University (LABIMA). The flume is 37 m long, 0.8 m wide, 0.8 m high and has no lid. It can accommodate water depths up to 0.6 m and it is equipped with a piston type wave maker that can generate regular and irregular waves up to $H = 0.3$ m for $T = 1.2$ s, with H the wave height and T the wave period.

The tested OWC model is depicted in Figure 1. It was built according to the Froude similarity, with a representative scale factor $1{:}50^{\text{th}}$. Methacrylate

was used in order to allow the observation of the phenomena occurring inside the OWC chamber. The OWC is fixed and has no degree of freedom.

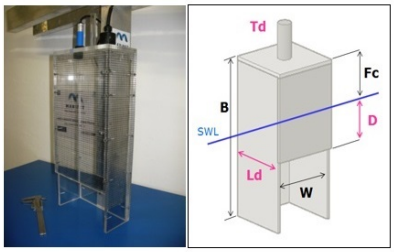

Symbol	Value[m]
Ld	0.08
W	0.186
B	0.45
D	0.22
Fc	0.12
Td	0.008

Figure 1: Picture and 3D schematic view of the OWC model and its dimensions.

The specific OWC characteristics, the adopted scale for the experimental model and the tested wave conditions have been selected according to previous studies [2, 18] conducted at LABIMA within the MARINET [19] project Laboratory that has served as testing infrastructures. The lateral wall thicknesses were 0.008 m while the back and frontal wall thickness were 0.01 m. The length of the OWC chamber (Ld) was 0.08 m (internal net value) and its width (W) was 0.186 m (internal net value). The back wall length (B) was 0.45 m and the lip draught (D) was 0.22 m. The freeboard (Fc) was 0.12 m. To impose a pressure drop that allow to make comparisons with the simulation, a hole on the OWC roof connected to a 0.08 m length pipe was used. The case of 0.008 m pipe diameter (Td) was tested, which represents 0.33% of the total area of the device's top part. The OWC model was located 22 m far from the wave maker and 15 m from the end of the flume. The flume bottom was horizontal and the water depth was 0.51 m, as illustrated in Figure 2.
The OWC model was equipped with an ultrasonic distance sensor to measure the internal free surface motion, a differential pressure sensor to measure the internal pressure oscillation and a hot wire anemometer to measure the air flow trough the vent. The ultrasonic distance sensor (Series 943-M18 F4V-2D-1C0-330E by HONEYWELL) has a declared accuracy of 10^{-3} m while the pressure transducer is a capacitive transmitter (Series 46X, by KELLER) with a full scale (FS) of 10^4 Pa and an accuracy of $\pm$ 0.1% FS. The hot wire anemometer was calibrated *ad hoc* in the range 0 to 10 m/s.
To measure the incident, reflected and transmitted waves, five ultrasonic distance sensors were used as Wave Gauges (WG) and were deployed along the wave-current flume as depicted in Figure 2. Table 1 summarizes the location of the wave gauges. The incident wave was measured during experiments where the OWC model was not in the flume and the data analysis was performed by using a time window during which the reflected waves coming from the end of the flume were not present. WG1, WG2 and WG3 were positioned in front of the OWC in order to obtain reflected waves by using reflection analysis algorithms as in [20]. WG4 was used to measure the free Surface oscillations of the water column inside the OWC model. WG5 was positioned behind the model

in order to measure the transmitted wave.

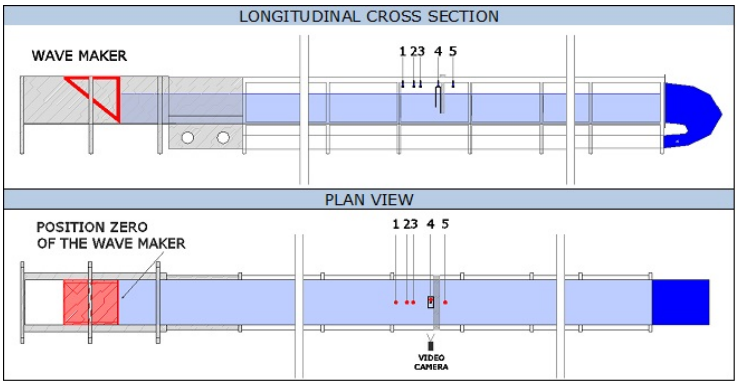

Figure 2: Position of the OWC model in the wave flume of Florence University. The OWC model is located 22 m far from the wave maker and 15 m far from the end of the flume.

Wave Gauge	Distance$[m]$
WG1	21.40
WG2	21.59
WG3	21.70
WG4	22.00
WG5	22.25

Table 1: Distances of the wave gauges from the wavemaker.

Stokes 2^{nd} order deep and intermediate water waves were tested. The wave parameters of the wave that will serve as a basis for comparison between laboratory experiments and numerical simulation is measured at WG3 (see Figure 2) in absence of the OWC model. The period $T = 1.4$ s and height $H = 0.042$ m.

3. Numerical model

3.1. Lattice Boltzmann Method

LBM solvers (see [21, 22, 23] for a detailed presentation of the model) are a popular alternative to traditional Navier-Stokes solvers such as finite-element and finite-volume methods. In particular, the method allows to handle complex geometries and physical ingredients (see [24] for instance) with a relative ease. No mesh-treatment of geometries is required: while mesh generation can be a critical process of other CFD methods, this step is usually quasi instantaneous in the lattice Boltzmann method. Indeed, the method is Cartesian mesh based and avoids building a body-fitted mesh around the provided geometry. Finally, the local nature of LBM makes it intrinsically parallelizable and suitable for massively parallel computing due to its excellent scalability [17].

LBM consists in solving the Boltzmann equation, a statistical equation for the kinetics of gas molecules [25], instead of solving directly the Navier-Stokes equations. Thus, the primitive variables solved for in the LBM represent the statistical particle distribution function, to which the usual macroscopic variables pressure and velocity relate as velocity moments, or "observables" in the sense of statistical mechanics.

The lattice Boltzmann equation can be derived by truncating the continuum Boltzmann equation in velocity space [26, 27]. At each lattice site, the LBM uses q particle distributions, also called populations, that are the discrete counterpart of the particle distribution function in the continuous case. We note $f_i(\mathbf{r}, t)$ the population that enters the lattice site $\mathbf{r}$ at time t with velocity $\mathbf{c_i}$. The q velocities $\mathbf{c_i}$ of the lattice are the quadrature points used for the Gaussian quadrature performed while discretizing the Boltzmann equation in the velocity space. It is common to characterize the lattice by noting DdQq its topology, with d the number of dimensions and q the number of velocities. A D3Q19 lattice has been used for this study.

The Bhatnagar-Gross-Krook (BGK) collision model [28] is a common way to approximates the collision term of the Boltzmann equation ; the single relaxation time lattice Boltzmann BGK equation reads:

$$f_i(\mathbf{r} + \Delta t \mathbf{c_i}, t + \Delta t) - f_i(\mathbf{r}, t) = -\frac{1}{\tau} \left(f_i(\mathbf{r}, t) - f_i^{eq}(\mathbf{r}, t) \right), \tag{1}$$

where f_i^{eq} is the equilibrium population, Δx and Δt are space and time steps of the lattice respectively, and τ the relaxation parameter. f_i^{eq} is obtained by expanding the Maxwell Boltzmann equilibrium distribution to second order in Mach number.

The macroscopic density and velocity can be computed from the populations as:

$$\rho = \sum f_i, \qquad \rho \mathbf{u} = \sum \mathbf{c_i} f_i. \tag{2}$$

One can show that the scheme above is equivalent to the incompressible Navier-Stokes equations in the limits of small Mach number through a Chapman-Enskog analysis [27].

The water surface is modeled as a free-surface with the VOF approach. In this approach, the mass of fluid in each cell is tracked and streamed along the lattice, and is used to compute the VOF value of the cell as the ratio between the mass and the density of the cell ; interface cells are cells with $0 < VOF < 1$. When the VOF value of a cell is greater than 1 (respectively lower than 0), then the cell is converted to a fluid cell (respectively an empty cell), and the surrounding appropriate cells become the new interfaces. More details about free-surface flow and an efficient LBM implementation of the free-surface model is proposed in [29, 30]. Because of the turbulent nature of the water flow, LES Smagorinsky correction [31] was used. The LB implementation of the Smagorinsky model can be found in [32, 33, 22].

3.2. Water-air coupling model

A crucial point is to model the influence water has on air as well as the influence air has on water due to pressure change into the chamber. Such a two-way coupling could be simulated using a 2-phase simulation. However, one can justify to not simulate the air dynamics by assuming that it does not affect the water behaviour significantly, although the *presence* of the air does, through the pressure exerted on the water surface. Hence, volume, pressure and mass are the only parameters of the air used in the model presented below. Air compressibility is not taken into account in this model, although further investigations should include these effects.

It should be emphasized that for sake of simplicity the PTO is modeled as a pipe in both the experiment and the simulation, in order to allow comparisons. However, the simulation models the PTO system in a general way by using a flow function j, whose form depends on the specific type of PTO used and typically is a function of the pressure gap between inside and outside the OWC chamber; in our case (pipe), one can assume that j corresponds to a Poiseuille flow, as it will be discussed below.

In order to implement the coupling, the mass of air into the virtual chamber is updated at each time step: $m(t + \Delta t) = m(t) + j(t) \cdot \Delta t$, with m the mass of air, Δt the time step and j the mass flow rate through the OWC exhaust system.

The water into the flume is surrounded by air at a constant atmospheric pressure p_0, while the pressure into the converter chamber is free to take a different value $p(t)$. From the Newton-Laplace equation $c_s^2 = \gamma p/\rho$, with c_s the speed of sound in the air, $\gamma \approx 1.4$ the adiabatic index of the air, and p and ρ the pressure and the density respectively, one can write the pressure as:

$$p(t) = \frac{c_s^2 \cdot m(t)}{\gamma \cdot V(t)}, \tag{3}$$

where $\rho = m/V$ has been used, with $V(t)$ and $m(t)$ the volume of air and the mass of air into the OWC chamber respectively. The air is assumed to be an ideal gas on the conditions that are of interest, and the mass flow rate through the turbine $j = -dm/dt$ is supposed to be a function of the difference Δp between p and p_0 : $j = F(\Delta p)$.

The precise form of j depends on the type of turbine used on the OWC. Thus, in absence of turbine-specific relation for function j, and since the experimental device exhaust is a pipe, we chose to roughly model the flow trough the numerical pipe using Poiseuille law: $j = \Delta p \cdot \pi R^4/(8\mu L)$, where μ is the kinematic viscosity of the air, and L and R are respectively the length and the radius of the pipe. The pressure $p(t)$, which is updated each iteration ($\Delta t = 5 \cdot 10^{-5}$ s), adapts very fast to the chamber conditions in comparison with the rate of change of $V(t)$, which has an amplitude of approximately 10^{-3} m^3 and a period of approximately 1 s. Thus, during a given interation, one can consider $V(t)$ to be constant. Writing Δh the change of surface elevation into the chamber during one semiperiod $T/2$, the change of surface elevation during one iteration

is therefore $\delta = 2\Delta t \Delta h / T$. A necessary condition for considering $V(t)$ as a constant during one lattice iteration then reads $\delta \ll \Delta x$. For the parameters used in this study, $\delta / \Delta x \approx 0.001$.

The differential equation for $m(t)$ defined by the previously cited Poiseuille law used in conjunction with formulation given in Equation 3 for $p(t)$ leads to the following formula for mass incrementation:

$$\Delta m = \Delta p \, \frac{1 - e^{-\alpha\beta \cdot \Delta t}}{\alpha}, \tag{4}$$

defining $\alpha = c_s^2 / (\gamma V(t))$ and $\beta = \pi R^4 / (8\mu L)$.

The following steps are performed at each iteration of the simulation:

1. Iteration of the lattice Boltzmann fluid.
2. Computation of the volume of air into the chamber by counting non-water cells into the volume defined by the converter.
3. Computation of the pressure using Equation 3.
4. Computation of the mass of air using the flow Equation 4 with the new pressure.
5. Impose the pressure to the free-surface below the converter, and go back to step 1.

Note that the above coupling scheme does not influence significantly the performances of the code. Indeed, its computational cost is of the order of the volume of air into the chamber (due to step 2 and 5); this is negligible compared to the computational cost of the LBM scheme for the fluid, which is of the order of the whole system volume (step 1 in the above scheme).

3.3. Simulation setup

All the simulations were based on the LB method, using the Palabos open-source library [34, 24] and a D3Q19 lattice. The 3D model for simulating water uses the BGK collision model in conjunction with a VOF approach, and simulates a viscous, incompressible fluid. The OWC geometry was implemented as a bounce-back boundary condition [35] as well as the walls of the flume. This corresponds to a no-slip macroscopic condition. The initial fluid condition was a fluid at rest everywhere on the domain, with a water depth of 0.51 m.

The real flume and OWC used in laboratory have been simulated numerically; their dimensions are the same, except for the virtual flume length that has been cut to 5 m only in order to save computational resources. Also, the virtual wave-maker is only 2 m away from the OWC, and it has been calibrated in order to produce waves that are similar to laboratory ones at the OWC location. The virtual waves are generated by applying a vertical force with variable amplitude on each cell of the fluid within a certain domain at the beginning of the flume. The period and amplitude of this force are used to tune the wave parameters. Any function can be considered for describing the intensity of the

force, and thus any combination of sin functions. However, we restrict here to simple sinusoidal waves, which correspond to a force on the form:

$$F(t) = A \cdot \sin\left(\frac{2\pi t}{T}\right), \tag{5}$$

where t is the time, T is the desired wave period in seconds and A is a constant amplitude. A calibration is necessary in order to link the wave height H to A. The calibration is done without OWC in the numerical flume. It consists in generating waves with the above described method for multiple values of A, and then to observe for each value of A the corresponding generated wave height at the OWC's center location. In this way, the curve $H(A)$ can be used for generating waves of desired amplitude. The force is applied on all fluid cells over an area of same width as the flume and on a length of 0.02 m just after the beginning of the flume, so that wave reflections occurring on the wall near the wave generator have a negligible delay in comparison with the wavelength of the produced wave (approx. 1 m). The boundary condition at the end of the flume allows the partial absorption of waves by imposing a maximum VOF value of 0.5 to all the interface cells just before the end of the flume. Nevertheless, some wave reflection can occur; however, due to their small amplitude and in conjunction with the numerical dissipation (see subsection 4.2), these waves quickly disappear and do not reach the OWC location. Figure 3 depicts the configuration of the system and shows the velocity norm everywhere in the domain.

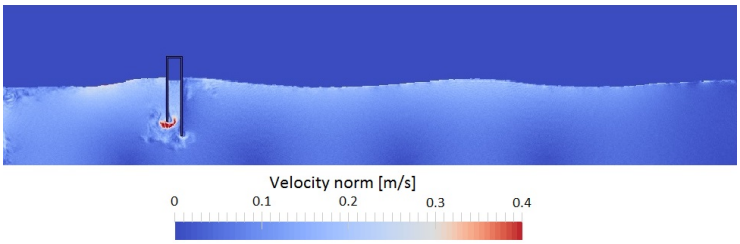

Figure 3: Velocity norm in the domain. The waves, propagating to the right, are produced on the left side of the flume, while the converter device is schematized in black. In this image, the OWC was located near from the wavemaker and does not correspond to the simulations. The flume is 5 m length, 1 m height and 0.8 m width.

The grid spacing used for the simulations was $\Delta x = 5 \cdot 10^{-3}$ m and the time step was $\Delta t = 5 \cdot 10^{-5}$ s. Consequently, the number of cells, given the real domain size, is approximately $3 \cdot 10^7$. For incompressible LBM flow, the value of Δt is chosen so as to keep the Mach number low. A ratio $\Delta x / \Delta t \approx 0.01$ has been shown to be an adequate value for the type of flow studied [21]. Computations were done by a distributed memory parallel machine. Each processing node is constituted of 12 cores sharing 24 Go RAM memory. The data presented here was processed by 96 cores distributed on 8 nodes. The computation time for one simulation of 10 seconds takes approximately 15 hours. Defining the speedup

value $S(n) = T_{seq}/T_n$ as the ratio between the time required by a sequential run of the simulation T_{seq} and the time required by a parallel run T_n using n cores, the speedup corresponding to simulations with 96 cores is approximately 60. Simulations using up to 144 cores have been run, giving a speedup of about 80, showing the good scalability of the computation. Figure 4 shows the speedup as a function of the number of cores.

To parallelize the code, the domain is divided into several parallelepipedic subdomains, each one running on a different processor. The number of cells per processor is distributed as homogeneously as possible. The values of the new populations and the macroscopic variables can be computed locally for each cell of any subdomain and are consequently updated in parallel. During the so-called streaming step, the populations are streamed along the lattice, and border cells of each subdomain has to be updated, requiring communications and data transfer between processors of adjacent subdomains. Thus, the amount of processor communications is proportional to the surface of the subdomains, while the amount of parallel computations is proportionnal to the volume of the subdomains.

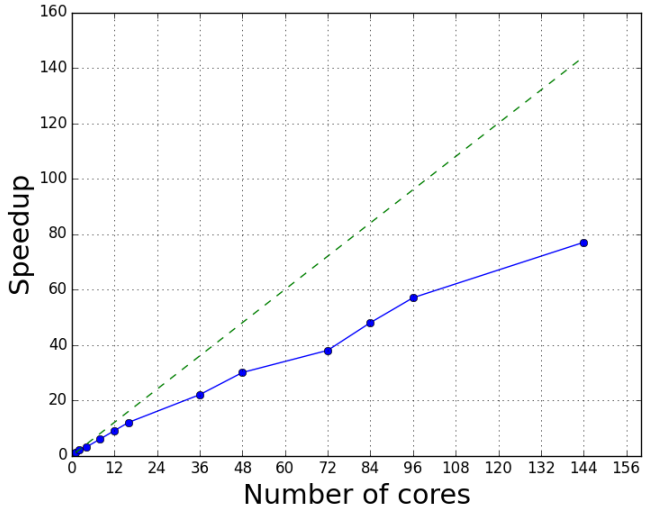

Figure 4: Speedup as a function of the number of cores. The linear behaviour indicates that the simulation can be scaled to more than 144 cores without wasting computational resources.

4. Validation of numerical waves

4.1. Dispersion

The virtual waves phase velocity and wavelength can be measured from the simulations and compared to the predictions from linear wave theory. According

to the dispersion relation (derivation can be found in [36] for instance), the phase velocity obeys the relation:

$$c = \sqrt{\frac{gL}{2\pi} \tanh\left(\frac{2\pi h}{L}\right)}, \tag{6}$$

with L the wavelength, g the gravity acceleration and h the water depth. Figure 5 compares data obtained from different simulations to the theoretical value obtained from the dispersion relation. All the tests were performed using the same simulation setup as presented in subsection 3.3, except that the virtual OWC device was removed and the flume length was extended to 10 m, so that the measurements can be done before reflected waves interfere with the measured waves. The tested waves height were comprised between $3.5 \cdot 10^{-2}$ m and $5 \cdot 10^{-2}$ m. To obtain phase velocity of a numerical wave, its crest is tracked each 0.5 m along a distance of 4 m, beginning 1 m far from the wavemaker. The phase velocity is the average value of the computed velocity on each step. The mean error of the numerical phase velocity compared to the theory is 0.03 m/s.

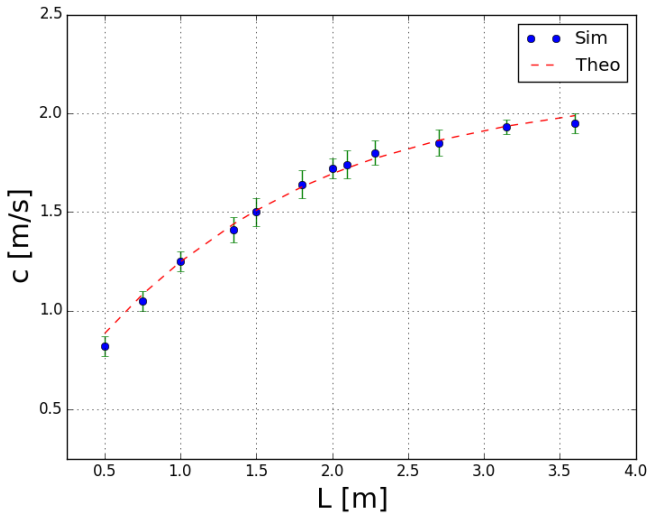

Figure 5: Phase velocity of the waves as a function of the wavelength. Theoretical value (dashed line) and data points from several simulations are compared. The mean error of the numerical phase velocity compared to the theory is 0.03 m/s.

4.2. Numerical dissipation

A numerical dissipation affects the simulated waves: typical wave (H = 0.042 m, T = 1.4 s) completely dissipates after approximately 10 m. A possible reason for that lies in the way excess mass from cells turning from interface to fluid and from interface to empty is managed in the LBM free-surface model.

Indeed, when the VOF value of a cell exceeds 1, the cell becomes a fluid cell, and the surplus of mass is redistributed on the adjacent interface cells [37]. The same applies for interface cells with VOF values less than 0, thus turning to empty, and the excess mass is negative. While this approach ensure mass conservation, it does not preserve momentum, which may be one reason for the dissipation observed. A way to improve it in the future would be to construct a mass redistribution scheme which explicitly imposes momentum conservation.

As a consequence of the dissipation, the wave height at the OWC location has to be calibrated with a simulation in absence of OWC device. The wave is calibrated on the location of the OWC's center, on the basis of the data from experiment done without the OWC. It is worth noticing that the grid is uniform, which means that although the lattice spacing $\Delta x = 5 \cdot 10^{-3}$ m appears small in comparison with the wavelength of the waves ($L/\Delta x \approx 10^3$), it still underresolves waves with height of the order of the centimeter: $H/\Delta x \approx 10$ in our case. However, to investigate water dynamics inside the OWC, the wave energy dissipation can be neglected in our case, since the typical size of the OWC is 0.1 m, while typical waves simulated dissipate in approximately 10 m.

5. Experimental and numerical models comparison

5.1. Water elevation comparison

Free oscillation test consist of measuring the oscillation frequency of the water into the converter as a response to an initial perturbation, which is in our case an initial water elevation of 0.05 m into the chamber. This test is done without waves attacks. We define as natural frequency the oscillation frequency of the water into the OWC for the conditions described above. Figure 6 shows the numerical and laboratory results. The laboratory experiment was performed by sucking the air from the pipe connecting the OWC vent with the outside, the internal free surface level was elevated up to +0.05 m with respect to the outside value. The air suction process was performed in about 2 s then the vent was closed, the system was set at rest and finally the vent was opened thus letting the internal water column oscillate while restoring the equilibrium state. The natural frequency is computed as the mean frequency obtained from the five first seconds of data shown in Figure 6. The values found are 0.91 ± 0.03 s^{-1} for the experimental case and 0.91 ± 0.04 s^{-1} for the numerical test. The difference between laboratory and simulation is mainly due to the turbine model used, which has a strong impact on the simulation. In our simulations, the Poiseuille law, applied to the pipe on the roof of the OWC, is a rough approximation that introduces a non-negligible bias in the way the air flow can discharge through the pipe. In addition to the above reason, the discrepancies arising at $t \approx 6$ s are due to the underresolution resulting from the fact that the amplitude of the oscillation becomes of the same order as the lattice space resolution Δx.

Figure 7 compares the water elevation into the converter for experimental and numerical cases at WG1, WG3, WG4 and WG5. The frequency of numerical wave inside the converter (WG4) is $f_{num} = 0.72 \pm 0.08$ s^{-1}, while the

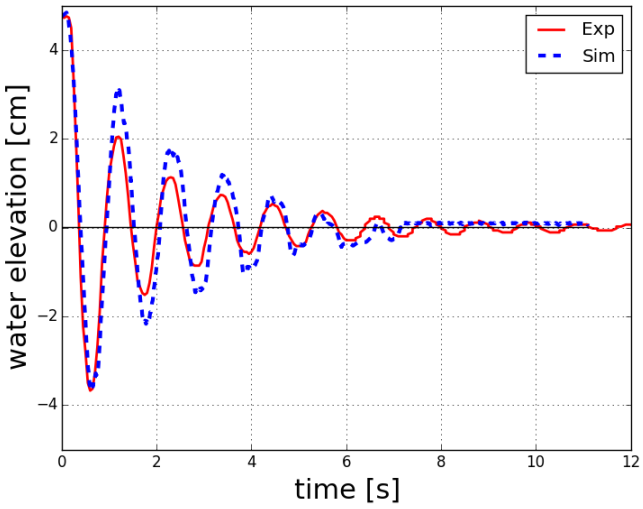

Figure 6: Water elevation into the converter (wave gauge 4) for free oscillation test. Natural frequency found are 0.91 ± 0.03 s^{-1} for laboratory test (plain line) and 0.91 ± 0.04 s^{-1} for simulation (dashed line).

experimental one is $f_{exp} = 0.72 \pm 0.02$ s^{-1}. The height of numerical wave inside the converter is $H_{num} = (3.77 \pm 0.45) \cdot 10^{-2}$ m, while the experimental value is $H_{exp} = (4.40 \pm 0.11) \cdot 10^{-2}$ m. The possible reasons for the observed discrepancies are given in section 5.2 below. The time here corresponds to the simulation time, since the wave generation process and the length of the real flume do not allow a direct data superimposition.

5.2. Pressure comparison

Figure 8 compares the relative pressure into the converter for experimental and numerical cases. As in Figure 7, the time indicated is the simulation time. The differences are mainly caused by the turbine model (as said above for free oscillation test), in conjunction with the numerical wave generation that produces waves slightly less smoothed than real ones. Indeed, since the pressure depends on the mass flow (*i.e* the time derivative of the water elevation) through the pipe, abrupt changes in the water elevation results in a strong noise of the pressure data. For this reason, the data for the mass of air contained into the converter along time has been used in order to reconstruct the pressure curve as seen in Figure 8, using the relationship established in section 3.2 between the mass of air and the pressure. The coupling model used has to be improved in order to smooth pressure changes that occurs at time scale of the order of $\Delta t << T$. Therefore, an average of the last few pressure values could for instance be considered in order to reduce the sensitivity of the pressure into the chamber to slight water motion. In addition, the function j used

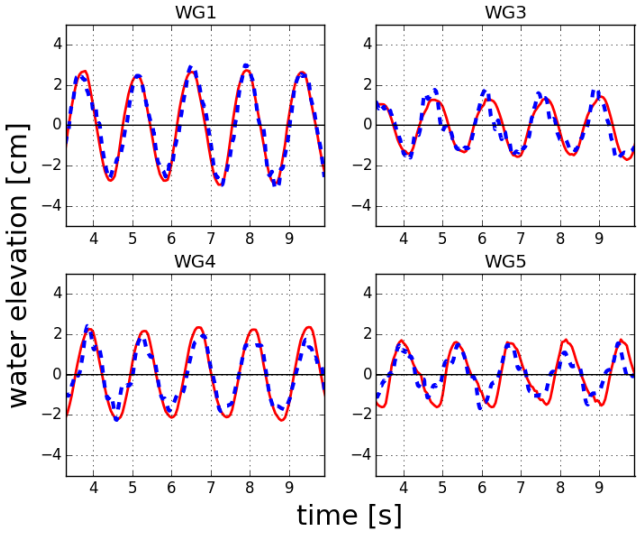

Figure 7: Water elevation at different locations for experimental (plain line) and numeric (dashed line) data under wave attack.

to model the PTO system should include more accurate physics. As seen in section 3.2, we assume a Poiseuille flow into the pipe in the present case, which could certainly be improved by taking into account the fact that the pipe has a finite length; indeed, the length of the so-called entrance region [38], in which the velocity profile develops until it reaches the expected parabolic one, exceeds the pipe length. Non-laminarity of the flow into the pipe may also be taken into account. Finally, remind that the air dynamics is not simulated due to the choice of a free-surface simulation, and compressibility effects are not taken into account, although they potentially influence the results [39].

6. Primary conversion efficiency of the numerical OWC

We give here the primary conversion efficiency of the numerical OWC, that we define (as done in [40] for instance) as the ratio between the energy of the air flowing through the pipe and the incoming water wave energy, both during one wave period: $\eta = E_{air}/E_{wave}$. Note that this definition totally excludes efficiency loss due to the turbine, as well as aerodynamic losses, since the air dynamics is not simulated in our model. Thus, the primary conversion efficiency does not reflect the actual efficiency of a real, turbine working OWC, but rather describes the loss of energy due to the conversion of wave motion into air motion induced by OWC geometry into the water.

The total power that the converter receives from water waves [36, 40] reads:

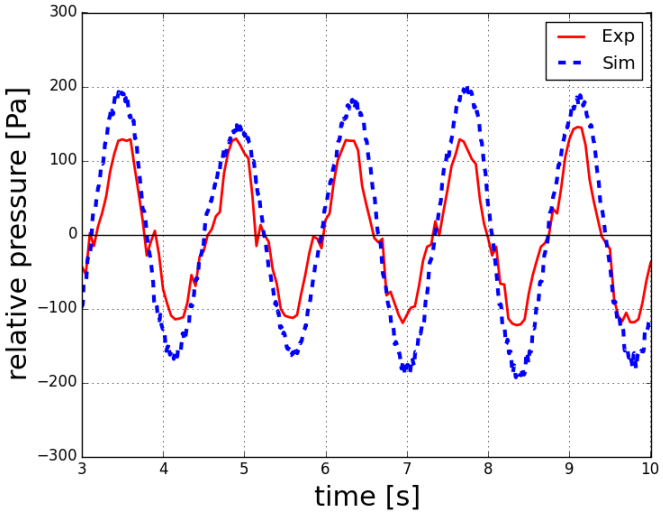

Figure 8: Relative pressure into the converter (wave gauge 4) for experimental (plain line) and numeric (dashed line) data under wave attack.

$$P_{wave} = \frac{\rho_{water} \cdot g^2 H^2 \cdot T \cdot W}{8\pi f(kh)}, \tag{7}$$

with $k = 2\pi/L$ and $f(kh) = 2\cosh(kh)^2/(2kh + \sinh(2kh))$.

The actual energy that a PTO system would receive can be seen as the kinetic energy of the air crossing the pipe of the converter, with constant section S_p. The air flows through the pipe with a mass flow rate $j(t)$. If the air velocity is $v(t)$ and ρ_{air} is the air density, one has the relation $j(t) = S_p \cdot \rho_{air} \cdot v(t)$, assuming the flow to be uniform and only along the pipe axis. The power of the air flow around the instant t is then the kinetic energy of the flow into the pipe by time unit, and can therefore be expressed as:

$$P_{air}(t) = \frac{1}{2} |j(t)| v^2 = \frac{1}{2} \frac{|j(t)|^3}{\rho_{air}^2 \cdot S_p^2}. \tag{8}$$

The above relation was used to deduce the conversion power of the numerical OWC at each iteration of the numerical scheme.

Figure 9 shows the primary conversion efficiency of the numerical OWC for different wave periods. For each case, the measurements have been done over four periods. The height of the incoming wave was measured in absence of the OWC device and was comprised between $4.4 \cdot 10^{-2}$ m and $5.1 \cdot 10^{-2}$ m. One can observe an efficiency peak of approximately 0.4 for period corresponding to the natural frequency experimentally and numerically found at $T \approx 1.1$ s, which is also consistent with value found by [16] for similar OWC design.

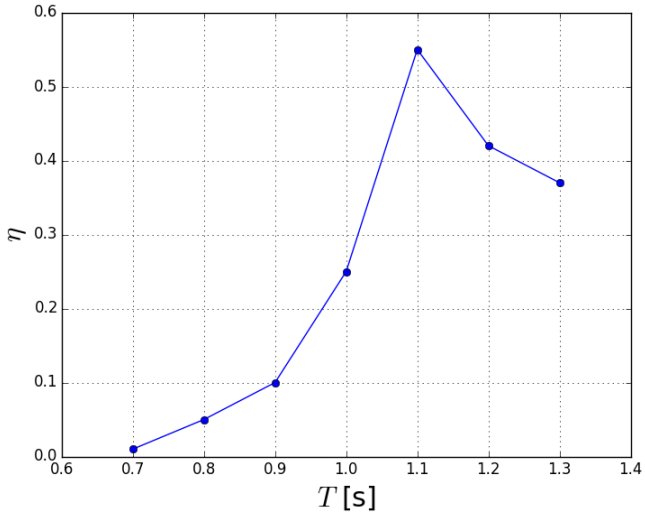

Figure 9: Primary conversion efficiency of the numerical OWC as a function of wave period. Wave height was comprised between $4.4 \cdot 10^{-2}$ m and $5.1 \cdot 10^{-2}$ m.

7. Conclusion

We have developed a novel approach for numerical simulation of OWCs that can serve as a basis for future works using LBM to the study of OWC devices. The model presented is sufficiently general to be applied on any arbitrary OWC shape, and any PTO as long as the function j, that relates the flow discharge to the pressure drop, is known. The OWC-LBM coupling algorithm has a negligible computational cost compared to the LBM numerical scheme. Although the simulations described in this article were intended to mimic experiments at 1:50 scale, the model can be immediately transposed to full-scale problems with no change, except adapting the lattice constants Δx and Δt to the new domain size and OWC size. The numerical model of the authors demonstrates the capability of the fully 3D LES free-surface model to investigate not only physical parameters into the converter but also full water dynamics outside the OWC. With this approach, the interaction between many OWCs, as it would be the case in a Large Floating Structure, is permitted. Moreover, as no assumption is done on the water waves nor the OWC geometry, this model allows the use of any complex OWC geometry, or any type of waves, as well as any arbitrary sea bed or obstacle in the domain.

The model can be improved in respect of the following points in order to achieve a better accuracy:

- The main weakness of the model is the numerical dissipation of waves, affecting their propagation. Investigations to find a more accurate model for LBM free-surface VOF model with respect to wave dissipation is needed.

Also, improvements can be achieved by using a refined grid near from the air-water interface [30]. Moreover, in cases where the water depth is much smaller than the wavelength, a coupling with a shallow-water model [37] could be envisaged before and after the OWC location, using the 3D free-surface model only at the OWC location.

- As described in subsection 5.2, the use of a flow discharge function j including more accurate physics, as well as the inclusion of compressibility effects, could result in a more accurate model and have to be investigated.

8. Acknowledgments

The research leading to these results has received support from MARINET[19], a European Community - Research Infrastructure Action under the FP7 'Capacities' Specific Program.

The computations were performed at University of Geneva on Scylla and Baobab clusters.

References

[1] A. Clement, et al., Wave energy in europe: current status and perspectives, Renewable and Sustainable Energy Reviews 6 (5) (2002) 405–431.
URL http://EconPapers.repec.org/RePEc:eee:rensus:v:6:y:2002:i:5:p:405-431

[2] D. Vicinanza, L. Cappietti, V. Ferrante, P. Contestabile, Estimation of the wave energy in the italian offshore, Journal of Coastal Research 64 (12) (2011) 613–617.

[3] V. Vannucchi, L. Cappietti, A. Falcão, Estimation of the offshore wave energy potential of the mediterranean sea and propagation toward a nearshore area, Proceedings of the 4th International Conference on Ocean Energy (ICOE), Dublin, Ireland (2012) 17–19.

[4] I. Lopez, J. Andreu, S. Ceballos, I. M. de Alegra, I. Kortabarria, Review of wave energy technologies and the necessary power-equipment, Renewable and Sustainable Energy Reviews 27 (2013) 413 – 434. doi:http://dx.doi.org/10.1016/j.rser.2013.07.009.
URL http://www.sciencedirect.com/science/article/pii/S1364032113004541

[5] B. Drew, A. Plummer, M. Sahinkaya, A review of wave energy converter technology, in: Proceedings of the Institution of Mechanical Engineers, Part A: Journal of Power and Energy, Vol. 223, 2009, pp. 887–902.

[6] T. V. Heath, A review of oscillating water columns, Phil. Trans. R. Soc. A 370 (2011) 235–245. doi:10.1098/rsta.2011.0164.

[7] R. P. F. Gomes, J. C. C. Henriques, L. M. C. Gato, A. F. O. Falco, Testing of a small-scale floating owc model in a wave flume, in: ICOE, 4th International Conference on Ocean Energy, 17 October, Dublin, 2012.

[8] S. Okuhara, M. Takao, A. Takami, T. Setoguchi, Wells turbine for wave energy conversion, Open Journal of Fluid Dynamics 3 (2013) 36–41. doi:10.4236/ojfd.2013.32A006.

[9] Y. Torre-Enciso et al., Mutriku wave power plant: from the thinking out to the reality, in: Proceedings of the 8th European Wave and Tidal Energy Conference, Uppsala, Sweden, 2009, 2009, pp. 319–329.

[10] T.J.T Whittaker et al., The LIMPET Wave Power Project - The First Years of Operation, http://web.sbe.hw.ac.uk/staffprofiles/bdgsa/shsg/Documents/2004sem/limpet.PDF, online; accessed 26 July 2015 (2014).

[11] A. F. d. O. Falco, Wave energy utilization: A review of the technologies, Renewable and Sustainable Energy Reviews 14 (3) (2010) 899–918.

[12] A. Iturrioz, R. Guanche, J. Armesto, M. Alves, C. Vidal, I. Losada, Time-domain modeling of a fixed detached oscillating water column towards a floating multi-chamber device, Ocean Engineering 76 (2014) 65 – 74.

[13] I. Lopez, G. Iglesias, M. Lopez, F. Castro, M. ngel Rodrguez, Turbinechamber coupling in an owc wave energy converter, Coastal Engineering Proceedings 1 (33).
URL https://journals.tdl.org/icce/index.php/icce/article/view/6572

[14] Z. Liu, B.-S. Hyun, K. yong Hong, Application of numerical wave tank to owc air chamber for wave energy conversion, in: Proceedings of the Eighteenth (2008) International Offshore and Polar Engineering Conference, Vancouver, 2008, pp. 350–356.

[15] U. Senturk, A. Ozdamar, Modelling the interaction between water waves and the oscillating water column wave energy device, Mathematical and Computational Applications 16 (3) (2011) 630–640.

[16] I. Simonetti, L. Cappietti, H. E. Safti, H. Oumeraci, 3D numerical modelling of oscillating water column wave energy conversion devices : current knowledge and OpenFOAM implementation (March 2016) (2015) 497–504.

[17] A. Peters, S. Melchionna, E. Kaxiras, J. Latt, J. Sircar, M. Bernaschi, M. Bison, S. Succi, Multiscale simulation of cardiovascular flows on the IBM Bluegene/P: Full heart-circulation system at red-blood cell resolution, in: Proceedings of the 2010 ACM/IEEE International Conference for High Performance Computing, Networking, Storage and Analysis, SC '10, IEEE Computer Society, Washington, DC, USA, 2010, pp. 1–10. doi:10.1109/SC.2010.33.
URL http://dx.doi.org/10.1109/SC.2010.33

[18] V. Vannucchi, L. Cappietti, Wave Energy Estimation in Four Italian Nearshore Areas, in: Volume 8: Ocean Renewable Energy, ASME, 2013, p. V008T09A007. doi:10.1115/OMAE2013-10183.
URL http://proceedings.asmedigitalcollection.asme.org/proceeding.aspx?articleid=1786696

[19] MARINET, http://www.fp7-marinet.eu, online; accessed 26 July 2015.

[20] E. P. D. Mansard, E. R. Funke, The Measurement of Incident and Reflected Spectra Using a Least Squares Method, Proceedings of 17th Conference on Coastal Engineering, Sydney, Australia. (1980) 154–172.
URL http://journals.tdl.org/icce/index.php/icce/article/view/3432/3112

[21] S. Succi, The Lattice Boltzmann Equation, For Fluid Dynamics and Beyond, Oxford University Press, 2001.

[22] B. Chopard, P. Luthi, A. Masselot, A. Dupuis, Cellular automata and lattice boltzmann techniques: An approach to model and simulate complex systems, Advances in Complex Systems 5 (2) (2002) 103–246, http://cui.unige.ch/∼chopard/FTP/CA/acs.pdf.

[23] S. Chen, G. Doolen, Lattice Boltzmann methods for fluid flows, Annu. Rev. Fluid Mech. 30 (1998) 329.

[24] A. Parmigiani, J. Latt, M. B. Belgacem, B. Chopard, A lattice Boltzmann simulation of the Rhone river, Int. J. Mod. Phys. C 24 (11) (2013) 1340008.

[25] S. Harris, An Introduction to the Theory of the Boltzmann Equation, Dover Publications, 1971.

[26] X. He, L.-S. Luo, Theory of the lattice Boltzmann method: From the Boltzmann equation to the lattice Boltzmann equation, Physical Review E 56 (6) (1997) 6811–6817. doi:10.1103/PhysRevE.56.6811.

[27] P. J. Dellar, Bulk and shear viscosities in lattice boltzmann equations, Phys. Rev. E 64.

[28] P. L. Bhatnagar, E. P. Gross, M. Krook., A model for collision processes in gases, Phys. Rev. 94 (1954) 511–525.

[29] C. Korner, M. Thies, T. Hofmann, N. Threy, U. Rde, Lattice boltzmann model for free surface flow for modeling foaming, Journal of Statistical Physics 121 (1-2) (2005) 179–196. doi:10.1007/s10955-005-8879-8.
URL http://dx.doi.org/10.1007/s10955-005-8879-8

[30] N. Threy, U. Rde, Stable free surface flows with the lattice boltzmann method on adaptively coarsened grids, Computing and Visualization in Science 12 (5) (2009) 247–263. doi:10.1007/s00791-008-0090-4.
URL http://dx.doi.org/10.1007/s00791-008-0090-4

[31] J. Smagorinsky, General circulation model of the athmosphere, Mon. Wheather Rev. 91 (1963) 99–164.

[32] S. Hou, J. Sterling, S. Chen, G. Doolen, A lattice boltzmann subgrid model for high reynolds number flows, Fields Institute Communications 6 (1996) 151–166.

[33] B. Chopard, M. Droz, Cellular Automata Modeling of Physical Systems, Cambridge University Press, 1998.

[34] Palabos, http://www.palabos.org, online; accessed 26 July 2015.

[35] X. He, Q. Zou, L. Luo, M. Dembo, Analytic solutions of simple flows and analysis of nonslip boundary conditions for the lattice boltzmann bgk model, Journal of Statistical Physics 87 (1997) 115–136.

[36] P. Kundu, I. Cohen, Fluid Mechanics, 4th Edition, Academic Press, 2008.

[37] N. Thürey, U. Rüde, M. Stamminger, Animation of open water phenomena with coupled shallow water and free surface simulations, in: Proceedings of the 2006 ACM SIGGRAPH/Eurographics Symposium on Computer Animation, SCA '06, Eurographics Association, Aire-la-Ville, Switzerland, Switzerland, 2006, pp. 157–164.
URL http://dl.acm.org/citation.cfm?id=1218064.1218086

[38] Y. Cengel, J. Cimbala, Fluid mechanics fundamentals and applications, McGraw-Hill, 2004, pp. 325–327.

[39] W. Sheng, F. Thiebaut, M. Babuchon, J. Brooks, A. Lewis, R. Alcorn, Investigation to Air Compressibility of Oscillating Water Column Wave Energy Converters, in: Volume 8: Ocean Renewable Energy, ASME, 2013, p. V008T09A005. doi:10.1115/OMAE2013-10151.
URL http://proceedings.asmedigitalcollection.asme.org/proceeding.aspx?articleid=1786694

[40] P. Koirala, S. Nagata, Y. Imai, T. Murakami, T. Setoguchi, Numerical analysis of primary conversion efficiency of oscillating water columns with multiple chambers, Procedia Engineering 105 (2015) 586–600. doi:10.1016/j.proeng.2015.05.036.
URL http://www.sciencedirect.com/science/article/pii/S1877705815008334